Atmos. Chem. Phys. Discuss., 6, 2853–2895, 2006
www.atmos-chem-phys-discuss.net/6/2853/2006/

Atmospheric Chemistry and Physics Discussions

Mesoscale circulations over complex terrain in the Valencia coastal region, Spain, Part 2: linking CO_2 surface fluxes with observed concentrations

G. Pérez-Landa[1], P. Ciais[2], G. Gangoiti[3], J. L. Palau[1], A. Carrara[1], B. Gioli[4], F. Miglietta[4], M. Schumacher[5], M. M. Millán[1], and M. J. Sanz[1]

[1]Fundación CEAM. Parque Tecnológico, c/ Charles R. Darwin 14, 46980 Paterna (Valencia), Spain
[2]Laboratoire des Sciences du Climat et de l'Environnement, UMR Commissariat à l'Energie Atomique/CNRS 1572, Gif-sur-Yvette, France
[3]Escuela Técnica Superior de Ingenieros Industriales de Bilbao, Universidad del País Vasco/Euskal Herriko Unibertsitatea, Bilbao, Spain
[4]IBIMET-CNR, Instituto di Biometeorologia, Consiglio Nazionale delle Ricerche, Firenze, Italy
[5]Max-Planck-Institut für Biogeochemie, Hans-Knöll-Strasse 10, 07745 Jena, Germany

Received: 22 December 2005 – Accepted: 31 January 2006 – Published: 11 April 2006

Correspondence to: G. Perez-Landa (gorkapl@confluencia.biz)

Abstract

Several consecutive vertical profiles of CO_2 concentration and meteorological parameters were collected during an intensive summer campaign in a coastal complex terrain region within the frame of the European Project RECAB (Regional Assessment and Modelling of the Carbon Balance in Europe). The region presents a marked diurnal cycle in the wind flow (analyzed in detail in a companion paper) as a consequence of the development of mesoscale circulations. In terms of the different stages of the diurnal cycle in the meteorology, these circulations result in an important coupling between atmospheric transport and surface CO_2 fluxes. To understand the effects of this interaction on the spatial variability of the observed CO_2 concentrations, we conduct a high-resolution simulation with a coupled biosphere-atmosphere model in the area of interest during a representative case study. Our model approach consists of estimating the regional NEE distribution by using a set of eddy-covariance measurements that are transported by a mesoscale model coupled to a Lagrangian particle dispersion model. Our simulations were able to successfully reproduce crucial processes controlling the mesoscale transport of CO_2. Availability of both simulations and observations for our analysis allowed us to characterize the influence of the coupling between mesoscale circulations and biological processes in the spatial gradients of the CO_2 concentrations. Temporal averages in the simulated CO_2 distribution show a 3-D rectification effect consisting of: 1) horizontally, a CO_2 deficit over land, mirrored by a CO_2 excess over the sea and 2) vertically, the prevalence of mean CO_2 depletion between 500 and 2000 m, and the permanent build-up of CO_2 in the lower levels.

1 Introduction

Carbon budgets can be quantified by combining atmospheric CO_2 measurements with an atmospheric-transport simulation model. This process, known as inverse modeling, is the usual basis for global transport models (Ciais et al., 1995; Fan et al., 1998;

ACPD

6, 2853–2895, 2006

Rayner et al., 1999; Bousquet et al., 2000; Gurney et al., 2002). However, the use of global transport models to infer continental fluxes introduces a number of limitations: (1) the model grid box does not represent a precise point-wise measurement, but rather an average concentration at a typical resolution of hundreds of kilometers; (2) these models do not realistically account for the heterogeneous nature of the surface fluxes, (3) they do not resolve small atmospheric scales that can be relevant in the transport and (4) they may not resolve the covariance of mixed-layer height with CO_2 fluxes and the pertaining "rectification" gradients .

To overcome these problems, several studies have used regional transport models with a typical grid of 30–50 km (Chevillard et al., 2002; Lin et al., 2004). In general, mesoscale models of this type produce a better agreement with CO_2 concentration data at continental sites than do global models. Nevertheless, over complex terrain, or if the CO_2 fluxes are very heterogeneous within the 30–50 km grid cell, many important transport features cannot be resolved. This supports the use of finer-scale mesoscale models that can be brought down to 1 km to better account for heterogeneous fluxes and transport and their interactions (Nicholls et al., 2003; Lu et al., 2005).

In this study, we use a fine-scale mesoscale atmospheric transport model to simulate the time-varying CO_2 distribution over the Valencia basin in eastern Spain. The area of study is a complex coastal terrain with spatially heterogeneous CO_2 fluxes. The model results are compared to CO_2 concentration measurements made during an intensive campaign to investigate the processes leading to CO_2 variability at various scales. Additionally, the use of CO_2 as a "tracer of opportunity" allows us to complement former studies regarding the effect of mesoscale processes in the transport conditions in the region (Millán et al., 1992, 1997; Gangoiti et al., 2001).

This study has four main objectives: (1) to test the performances of a fine-scale transport model over a complex terrain region, using CO_2 as a tracer (2) to quantify the 'rectification' of vertical and horizontal coupling between atmospheric transport and diurnal CO_2 flux variability in the presence of mesoscale processes, yielding interesting effects such as CO_2 layering, (3) to determine the contribution of distinct regional CO_2

sources to the observed CO_2 concentration signals and variability and (4) to use the model to simulate the CO_2 distribution within the whole Valencia region, in order to gain knowledge about how local processes are transmitted to the regional scale.

In the study we begin by describing the CO_2 concentration measurements and the surface flux measurements made during the campaign (Sect. 2). Then we recall the main results of the mesoscale dynamical simulation (see also Perez-Landa et al., this issue). We describe the Lagrangian particle dispersion model that serves to transport CO_2 using these dynamical fields, as well as the simple model that we used to map the distribution of biotic and fossil CO_2 fluxes (Sect. 3). We discuss the modeled and observed CO_2 variability at local (Sect. 4) and regional scales (Sect. 5) in terms of the coupled daily cycle of both mesoscale and biotic processes. Finally, we analyze the effects of these processes on the temporal averages of the simulated CO_2 distribution in the Valencia region (Sect. 6).

2 Observed fluxes and CO_2 concentrations during the campaign

The two-week experimental campaign took place near the city of Valencia in the summer of 2001, as part of the European project RECAB (see www.bgc-jena.mpg.de/public/carboeur/projects/rec.html). During the campaign, we made: (1) airborne CO_2 concentration measurements, both on horizontal transects near the surface and on vertical profiles (at repeated intervals during the day), (2) airborne eddy-covariance CO_2 flux measurements on the horizontal transects and, (3) eddy-covariance flux measurements at two representative ecosystem sites. In addition, we collected other supporting data to be used to interpret the CO_2 signals, in particular meteorological observations airborne and at a network of surface stations and eddy covariance fluxes of water vapor and energy. The latter datasets, together with the atmospheric circulation patterns during the campaign, were described in the companion paper by Perez-Landa et al. (2006) (referred to as P06). We focus our analysis on 2 July, a day that was representative of the typical development of mesoscale circulations (see P06) and that

ACPD
6, 2853–2895, 2006

EGU

provided a sufficient number of measured profiles to characterize the diurnal cycle of the processes.

2.1 Airborne CO_2 concentrations

The aircraft routes during the 2 July campaign are detailed in Fig. 1. In-situ measurements of CO_2 were collected onboard a Sky Arrow aircraft by means of a LICOR 7500 open-path infrared analyzer operating at 50 Hz (Gioli et al., 2004). Twelve horizontal CO_2 measurement transects were made at either 25 m or 50 m above ground level near the Mediterranean coast, predominantly over rice-paddy landscapes (Fig. 1). Vertical profiles of CO_2 were taken between 25 m and 800 m at 06:23, 07:40, 11:47 and 13:03 UTC over a rice paddy-field at the northern edge of the horizontal transects, south of the city of Valencia (see Table 1 in P06). Flask sampling was also carried out with an additional airplane above an area dominated by citrus orchards, about 5 km west of the rice field site (Fig. 1). The flights began at 07:43, 11:21 and 14:51 UTC with sampling at five discrete heights between 100 and 1500 m. Subsequently, the flasks were analyzed at the Max Planck Institute for Biogeochemistry in Jena (Germany) for the mixing ratios of CO_2, N_2O, CH_4 and for the stable isotopes in CO_2 (Schumacher, 2005).

2.2 Airborne and ground-based eddy covariance fluxes

Airborne fluxes of CO_2 and H_2O were measured during each horizontal transect, using a 3 km space length and applying methods described in Gioli et al. (2004). Ground-based continuous eddy covariance measurements are made at a pine forest called El Saler (SA) and at a rice paddy-field (RI). Both sites are located in close proximity to where the vertical profiles were sampled (Fig. 1). The SA flux tower (15.5 m) has been operational since 1998, and measures a dense natural maquia canopy (1–2 m), with an overstorey dominated by Pinus halepensis trees (50 to 100 years old and approximately 12 m in height). Soil is sandy, well-drained and classified as arenosol calcareous (FAO,

1998). The rice paddy flux tower (2 m), located above a rice canopy of about 60-cm in height, was set up only for the duration of the campaign. Soil is clay loam (upper horizon, 0–30 cm) and silty clay loam (deeper than 30 cm) and is classified as fluvisol calcareous (FAO, 1998). For eddy covariance measurements, wind velocity and temperature fluctuations were measured with a 3-D ultrasonic anemometer (model Windmasterpro, Gill Instruments Ltd., Lymington, UK), and H_2O and CO_2 fluctuations were measured with a closed-path infrared gas analyzer (IRGA; model LI-6262, Li-Cor Inc., Lincoln, USA). Data were collected at a 20 Hz sampling rate and 30-min fluxes were calculated using eddy-covariance software (Alteddy 1.2, Alterra Green WorldResearch, Wageningen, The Netherlands). The eddy system and data processing followed the standard Euroflux methodology (Aubinet et al., 2000). Supporting meteorological measurements were performed at SA and stored as 10-min averages. They include incoming photosynthetically active radiation (PAR) (LI-190SA Quantum sensor, Li-Cor Inc., Lincoln, USA) and air temperature (AT1 Thermistor, Delta-T Devices Ltd, Cambridge, UK).

3 Models of CO_2 fluxes and transport

3.1 Atmospheric dynamical model

The atmospheric transport of CO_2 is simulated using prescribed surface fluxes from a simple model (see Sect. 3.2) and the 3-D dynamical fields pre-calculated from the RAMS atmospheric mesoscale model. The RAMS model is described in P06, and here we only recall the main model input data and simulated circulations. The RAMS 4.3.0 non-hydrostatic model was nested three times with increasing horizontal grid spacing, starting from the whole western Mediterranean region and going down to the campaign domain bounded by 1 W, 38.8 N and 0.4 E, 39.9 N (Fig. 1). Within the campaign domain, the model horizontal resolution is 1.5 km, and its vertical grid spacing increases gradually from 30 m to 1000 m, with the model top being 17 000 m. There are 15 lev-

els in total below 1000 m. The model is forced at the lateral boundaries of its largest nesting domain by large-scale meteorological analyses (Caplan et al., 1997). Soil temperature and soil moisture are initialized from a spin-up simulation, starting two months before the campaign period. The results in P06 indicate that the principal dynamical mesoscale features successfully reproduced by RAMS for the campaign episode were:

1. the nocturnal drainage flow driven by terrain shape and gravity
2. the morning sea-breeze development and inception of up-valley breezes
3. the early-afternoon, "combined-breeze", an organized mesoscale circulation, where air parcels become sucked inland, uplifted on mountain slopes, and return seawards at altitudes lower than 3 km
4. the southward shift in the breeze flow during the late afternoon of 2 July.

3.2 Net Ecosystem Exchange (NEE)

We constructed a simple NEE model derived from the eddy covariance observations and freely inspired by (Gerbig et al., 2003). At each grid point, NEE depends both on radiation in the photosynthetically active domain (PAR) and on vegetation type. Three different dominant vegetation types are considered: Rice, Citrus, and Mosaic. We established a correspondence between the land cover information from the pan-European CORINE database at 50 m resolution (CEC, 1995) and each one of the three above types. Rice vegetation covers 15 000 ha in the model domain (5% of flat areas) and is treated separately for the NEE modeling. Rice is an irrigated and highly productive crop, with a higher daytime-NEE uptake than other ecosystems. Rice paddies are just under the aircraft profiles, and thus will influence strongly the CO_2 concentration signals there (see Sect. 4). Citrus vegetation corresponds to the many orange tree plantations in the Valencia region, referred to as "Fruit trees and berry plantations" in the CORINE database. Citrus is the dominant vegetation type on the

ACPD
6, 2853–2895, 2006

coastal plains, and it covers an area of 269 000 ha, i.e. 68% of flat terrain areas. Mosaic vegetation represents all other plant types, chiefly "Complex cultivation patterns" (20%), "Coniferous forest" (20%), "Sclerophyllous vegetation" (35%) and "Transitional woodland-scrub"(17%), which together cover 69% of the total domain, but 95% of the mountainous areas.

Our strategy for modeling NEE was to determine a common set of parameters for each vegetation type, based on the flux tower measurements. The NEE model equations are

$$\text{If daytime}: \quad NEE = c_i - \frac{a_i \times PAR}{(1 - PAR/2000 + a_i \times PAR/b_i)} \tag{1}$$

$$\text{If nighttime}: \quad NEE = c_i \tag{2}$$

Where a_i and b_i are constants determined from each type i of vegetation by a least-square fit to quality-checked half-hourly daytime NEE data, and c_i equates the mean night-time observed NEE, i.e., respiration (see Table 1). Equation (1) is similar to the one used by Falge et al. (2001) and follows a typical Michaelis and Menten (1923) hyperbolic shape. The value of c_i is determined from the nighttime eddy-covariance measurements, but it is also used for daytime conditions. Thus we neglected daytime changes in respiration (e.g., Atkin, et al., 2005).

Rice vegetation parameters are inferred from the eddy-covariance data of 1–2 July (Fig. 2b) at the RI tower (Fig. 1) and their values are reported in Table 1. The modeled NEE for Rice at mid-day shown in Fig. 3 is in good agreement with the independent airborne flux measurements shown in Fig. 4., a feature already pointed out by Gioli et al. (2004). Parameters for the Citrus vegetation could not be determined during the campaign, and we used instead eddy-covariance fluxes measured in a nearby site in July 1995 (Seufert et al., 1997).

For the Mosaic category, however, we lacked direct eddy-covariance data. At SA, the vegetation is relatively similar to that of the Mosaic category, but its greater proximity to the sea creates milder and wetter conditions (due to the breeze regime) than over

most of the inland Mosaic-covered regions. Therefore, to constrain the model parameters for Mosaic vegetation, we selected the driest NEE episodes registered at the SA tower. We identified 11 days between mid-June and mid-August 2001, during which the mesoscale conditions consisted of dry and warm westerly winds (Foehn episodes at the lee of the coastal mountain range) prevailing in the absence of a sea breeze. Under such anomalous warm and dry conditions, the measured NEE at SA was on average lower than under normal conditions. The daytime NEE at optimum PAR used for the Mosaic (Fig. 2a) is, for instance, 62% lower than the "normal" SA values NEE measured during sea-breeze conditions.

These NEE patterns are extrapolated to the whole domain using vegetation type maps (see above) and PAR variations. The point-wise PAR measurements from the SA site were assumed to be representative of the whole domain under clear sky conditions (as was the case during the campaign). The resulting NEE temporal variations for each vegetation type are illustrated in Fig. 3.

3.3 Fossil fuel emissions

Urban areas cover 3% of the campaign domain and 7% of the flat area. The Valencia region has a population of 1.4 M inhabitants, mostly located in the city of Valencia (0.8 M inhabitants). It should be kept in mind that this major CO_2 fossil fuel source is located just 10 km north of the vertical profiles. Detailed regional CO_2 fossil fuel emission inventories do not exist. Thus, we desegregated the annual mean fossil fuel CO_2 emissions reported at the 1° spatial resolution for the year 1995 in the EDGAR 3.2 global inventory (Olivier et al., 2001) over the campaign domain and increased this by 22% in order to account for rising Spanish trends between 1995 and 2001 (Marland et al., 2003). All the fossil fuel CO_2 emissions in the EDGAR 3.2 grid cell containing Valencia are distributed in the city of Valencia (75.9 km^2), disregarding smaller cities and roads. This gives an emission rate of 4.76×10^9 gC day^{-1}, which corresponds to a flux of 62.7 gC m^{-2} day^{-1} in the city area. This value is much stronger that the mean daytime NEE uptake flux by vegetation of –3.73 gC m^{-2} day^{-1} for the whole domain (see Fig. 3).

ACPD
6, 2853–2895, 2006

A mean diurnal cycle is assigned to the fossil fuel CO_2 emissions by using data from the Valencia-city air quality network. We estimated the diurnal cycle of fossil fuel combustion processes (mainly car traffic), and therefore of fossil fuel CO_2 emissions, by using normalized hourly carbon monoxide atmospheric concentration measurements from three representative air quality stations located inside the city over the period 1996–2001 (see data at http://www.cth.gva.es/cidam/emedio/atmosfera/index.htm). The resulting fossil fuel CO_2 emissions shown in Fig. 3 show two pronounced peaks at around 07:00 and 17:00 UTC, corresponding to road-traffic rush hours.

3.4 Lagrangian particle dispersion model

We transport CO_2 using dynamical fields pre-calculated by RAMS and the HYbrid Particle And Concentration Transport (HYPACT) Lagrangian particle-transport model (Tremback et al., 1994 and Walko et al., 2001). The HYPACT model was formerly applied to the Mediterranean region by Gangoiti et al. (2001 and 2002) and by Kotroni et al. (1999) to study the regional transport of pollutants. It was also used to diagnose the vertical injection of aerosols in the Alps (de Wekker et al., 2004) and assess the importance of meteorological scales in air pollution forecasting over a coastal complex terrain area on the east coast of Spain (Palau et al., 2005).

By construction, the HYPACT particle dispersion model has the same domain configuration and nesting capabilities as RAMS, allowing us to prescribe surface sources at the RAMS maximum grid cell resolution, with either continuous or sporadic releases of particle packets. The three wind and TKE turbulence-field components are extracted from the RAMS output every 10 min and then used to drive the HYPACT model. In HYPACT, particle transport is calculated from interpolated RAMS fields every 30 s, starting 30 h before collection of the first vertical profile at 06:23 UTC on 2 July and continuing for 48 consecutive hours following emission. Particle transport and dispersion are computed within the three nested domains, allowing to capture simulation of recirculations of particle packets with veering winds. Note also that the Mosaic vegetation source regions are partly located outside the smaller model domain (Fig. 1) and are

thus sending particles inside, which (partly) accounts for external regions contributing to CO_2 variations inside.

3.5 Source regions

Due to computing-power limitations, particles are not released from each RAMS grid cell but rather from a number of large source regions, as shown in Fig. 5. There are 18 different vegetated regions and one urban region. The contour of each region (Fig. 5) is chosen (1) to be spatially coherent with dominant vegetation types, (2) to follow relevant terrain/flow information, and (3) to have a simple geometry. We chose, for instance, the five Citrus source regions with their symmetry axis parallel to the main valleys, so that particles from these regions would form distinctly identifiable streams when drained by nocturnal winds. The source regions get smaller nearer to the vertical profiles site over the rice paddies. Thus, we have small Rice source regions (mean individual area of 29.9 km^2), intermediate-size Citrus regions (310 km^2), and large Mosaic regions (1266 km^2). The simple geometry selected for the source regions, however, leaves some gaps in area, shown as white areas in Fig. 5, with the result that the sum of the 19 regions covers only 78% of the inner domain. In order to avoid losing mass from these uncharted areas, we enhanced particle emissions from each source region by a scaling factor dependent on vegetation type, so as to match the total flux prescribed for that vegetation category.

3.6 From particles to concentration

Particle release is simulated as follows: (1) spatial emission patterns are "uniform" with emitted particles grid points changing randomly each 20 s, (2) temporal patterns change every 30 min, and follow the NEE diurnal cycle given in Fig. 3. The CO_2 concentration pertaining to each regional source is obtained by dividing the number of particles found in a "detector" grid box by the corresponding number of moles of dry air simulated by RAMS. We keep track separately of CO_2 concentration changes caused

ACPD
6, 2853–2895, 2006

EGU

by particle packets emitted during each 30-min interval. Each particle is assigned a mass of 300 gC so that at least 20 particles equate a concentration change of 1 ppm, the typical precision of airborne CO_2 measurements (see Appendix A1). Given the mass of each particle, for 19 regions multiplied by 96 separate concentration fields (30 min release intervals during 48-h), we calculated the dispersion of 29 million particles in total, which represents 14 days of CPU time on a 2 GHz local lab-top computer.

4 Observed and modeled CO_2 vertical profiles driven by mesoscale processes

Figures 6a–d shows the observed concentration of CO_2 and the vertical profiles for potential temperature, water vapor, and horizontal winds. For the meteorological variables, their detailed analysis is made by P06. Thus, we only briefly recall here what is important for understanding the CO_2 signals. A temperature inversion very near the ground is observed in the earliest profile at 06:23 UTC. The potential temperature profile indicates some vertical mixing below an inversion located at 200 m above the surface (Fig. 6c) in the 07:40 UTC profile. The sea breeze circulation becomes established soon afterwards, and the next two profiles at 11:47 and 13:03 UTC show evidence of a mixed layer below 200 m (Fig. 6c). Above that height, stable conditions persist and are reinforced during the afternoon by the compensatory subsidence over the coast (discussed in P06). The solid circles in Fig. 6a represent the CO_2 measurements made taken on air samples above citrus orchards west of the Rice fields (Fig. 1). Despite the different location of both aircrafts, a gradual decrease in CO_2 concentrations in the lower levels can be observed during the course of the day, and this is similar to the continuous profiles.

A direct comparison between observed and simulated CO_2 vertical profiles is not possible because of differences in the timing, location and magnitude of the signals. Such biases can be due to the assumptions made in the modeling approach. Among others, in our simulation, only the local CO_2 signal is considered, while former studies on pollution transport have documented a large-scale regional transport capable

of advecting stable layers of pollutants over the Mediterranean basin (Gangoiti et al., 2001). Additionally, the impact of model limitations on either the parameterization of turbulence or the representation of layers at a feasible vertical resolution can seriously affect the results.

Thus, in the Fig. 7 comparison between the modeled and the experimental CO_2 vertical structure, the performance of the model should be evaluated in terms of its ability to reproduce the main observed features, resulting from characteristic meteorological and biological processes. In this figure, the modeled CO_2 concentration is horizontally averaged over a 3-km radius around the aircraft profile site. However, simulated CO_2 is plotted vertically at the model's maximum resolution of 5 m. The contribution from different source regions and from sources and sinks acting at different time intervals are also given in Fig. 7. A different color is used for each region and a different color density for each time interval, with darker color for more recently emitted CO_2.

Considering that the governing meteorology is associated with a daily periodicity in the wind circulations, we have divided the one-day measurement period into three different consecutive stages in order to analyze the changes in the CO_2 vertical distribution. All times are expressed in UTC units.

4.1 Nocturnal regime

During nocturnal hours, respired CO_2 merges with stable drainage winds flowing towards the sea. The 06:23 profile shows a higher CO_2 concentration in the lowest 100 m than aloft. These signals correspond to a pool of respired CO_2 trapped inside the near-ground thermal inversion still present at this time of the day. This pool is advected towards the sea by drainage of katabatic winds (Figs. 6a–b). The observed near-surface CO_2 build-up amounts to 30 ppm; a back-of-envelope calculation in which 3.6 μmol $^{-2}$ of CO_2 (i.e., the Rice-vegetation-respired CO_2 flux in Table 1) are injected into a 100 m-thick surface layer for 8 consecutive nocturnal hours, gives a CO_2 accumulation of 29 ppm, very close indeed to the observed one. The simulated vertical profile in Fig. 7 shows a near-surface CO_2build-up of 10 ppm. The CO_2 drainage pool is pre-

ACPD
6, 2853–2895, 2006

EGU

dominantly composed of molecules respired during the previous 5 h, or even before, coming from Mosaic and Citrus vegetation source regions. Superimposed on these drainage effects, there is a small negative contribution of 1 ppm caused by the recent CO_2 uptake over Rice since sunrise (see Fig. 3).

4.2 Transition between nocturnal and diurnal regimes

At 07:40 UTC, i.e. three hours after sunrise, the transition between drainage winds and sea breeze inception occurs. This period is characterized by very low wind speeds (Fig. 6b). Photosynthesis and vertical mixing by turbulence act to decrease CO_2 in the lowermost part of the profile. Between 06:23 and 07:40 UTC, we observed a CO_2 decrease of 15 ppm, which would correspond exactly to the removal of CO_2 by the NEE of Rice vegetation (Table 1) from a 100 m thick surface layer. Just above the shallow surface layer, we can see some variability in the CO_2 profile, with occasionally higher values than at 06:23 (Fig. 6a). This likely reflects the uplifting of respired CO_2 by vertical transport processes in large convective eddies. In the model, the wind speed weakens at around 07:00, a feature which is in good agreement with the observed transition to sea breeze flow (see Fig. 8). During the transition, the modeled vertical mixing intensifies in the lowermost 300 m of the air column (Fig. 7). At 07:40, we simulate small positive and negative CO_2 contributions below the top of the mixed layer. CO_2 is removed continuously by photosynthesis from nearby Rice and Citrus regions (Fig. 7).

4.3 Diurnal regime

This third stage is associated with the development of the breezes directed inland while photosynthesis is taking place. At 11:47, the sea breeze was already developed (see winds in Fig. 6b) and, as a result of photosynthetic uptake, generated an additional 15 ppm decrease in CO_2 as compared with the earlier profile measured. The profile measured between 200 m and 300 m shows a very interesting feature: a layer depleted of CO_2 by about 30 ppm (Fig. 6a). This layer is not apparent in the wind and H_2O pro-

files. Above this layer, the CO_2 builds up forming a "hump" of 15 ppm at a height of 400 m. By 13:03, the layer has disappeared, but variations of up to 5 ppm persist throughout the profile. Due to photosynthesis, a continual decrease is observed in the CO_2, amounting to 5 ppm since the former profile at 11:47. The model results show that the simulated breezes advect CO_2 inland; therefore, no land source region contributes to the CO_2 simulated concentrations for the 11:40 profile, as seen in Fig. 7. Thus, the simulated CO_2 vertical distribution is homogeneous, although close to the surface some Rice uptake signal persists, contributing a negative 2 ppm gradient locally. Between 13:00 and 13:40, the modeled CO_2 profile shows a continuing decrease in CO_2 below 200 m, due to Rice uptake. At this time of the day, that is two hours after the 30 ppm measured depletion, the model produces a CO_2 layer depleted by 6 ppm at ≈500 m, displaced upwards between 13:00 and 13:40, and summing up to a total negative anomaly of –13 ppm (Fig. 7). It is encouraging to see that a high-resolution model can simulate the layering in the vertical CO_2 concentration. It is also interesting to note that both the observed and the simulated profiles show a high temporal variability (Fig. 7). By 13:00, the modeled layer contains the dominant signature of the recent Rice vegetation uptake to which the air mass was exposed. Later on, at 13:40, it receives additional contributions from uptake over Citrus and Mosaic vegetation (Fig. 7). Interestingly, we simulate a positive CO_2 contribution from Mosaic regions (+3.5 ppm in Fig. 7) in the layer. This feature reflects the fact that the 50% of sources were active during the previous 5–10 h, plus those active 10–15 h prior, i.e., the respiration from the former night. The last vertical CO_2 profile simulated at 15:40 contains a strong contribution from Rice vegetation uptake near the ground. In the lower 150 m, there is also a positive CO_2 signal of +5 ppm emitted by Citrus, Mosaic and Urban sources more than 15 h before. Above 900 m, there is a negative variation in the simulated CO_2 of –5ppm, reflecting the action of Citrus and Mosaic vegetation sinks that were active during the previous 5 h.

ACPD
6, 2853–2895, 2006

5 Basin-scale changes in CO_2 distribution driven by mesoscale processes

We now use the spatial and temporal coverage of the model output to understand the causes of CO_2 variations in the Valencia basin. The time-varying vertical distribution of the $CO_2$and of the horizontal winds is shown in Fig. 8. Figure 9 shows the CO_2 distribution near the surface (0–30 m), as well as the streamlines that represent the 15-m wind fields. In both cases we added a constant offset value of 366 ppm to the positive or negative simulated time-varying CO_2 concentration signal. This offset is chosen to be equal to the average CO_2 value measured at the top of the four profiles taken during the campaign. At the nocturnal stage (Fig. 9a), the land drainage flows with elevated CO_2 values (up to 376 ppm) penetrate over the sea. In Fig. 9a, the maximum simulated values of CO_2 are estimated at 06:00 downwind of the Valencia city. The city plume of fossil fuel CO_2 adds to the convergence of respired CO_2 streams channeled by the Xucar and Turia valleys to produce a large "tongue" of CO_2-enriched air that extends more than 100 km away from the coast. At 06:00, the first effects of photosynthetic uptake appear over the sunny slopes of the mountains outside the main valley flows. This translates into lower near-surface CO_2 values (Fig. 9a).

At 08:00, during the transition between regimes, solar heating of the eastern slopes facilitates the rapid development of local valley breezes. However, close to the coast and offshore, the CO_2 drainage pool formed during the night is still notably present (Fig. 9b). The grey lines in Fig. 9b showing the convergence of horizontal winds at 08:00 indicate that vertical injection has started to occur locally. The wind streamlines show a very complex circulation in which the scales of the processes are related to each valley's size and shape. Note also that there is a wind divergence from the center of each valley. Photosynthetic uptake has the effect to strongly decrease CO_2 concentrations over land at 08:00 as compared to the previous 06:00 time interval. Given the shallow mixed layer height at this time, the CO_2 near the surface drops abruptly from its highest to its lowest values of the day within the 2 hour-period between 06:00 and 08:00 (compare Figs. 9a and b). A generalized wind reversal from seaward to

ACPD
6, 2853–2895, 2006

EGU

landward, seen clearly in Fig. 8, precludes the advection of this CO_2 uptake signal towards the sea. Thus, offshore elevated CO_2 concentrations are preserved into a stable "drainage lake" containing CO_2 respired from the former night.

Later in the morning, at 11:00, the sea and valley breezes begin to merge into a "combined breeze" (Fig. 9c). The combined-breeze circulation extends from over the sea where the winds diverge, up to the coastal mountain ridge parallel to the coast where the winds converge (see discussion in P06). In the northern part of the Valencia, the convergence line is situated more remotely from the coast and lies outside the campaign domain shown in Fig. 9 (this feature was diagnosed from the simulation in the next coarser nesting domain, not shown here). The "drainage lake" of the respired CO_2 night gets diluted up and swept back by breeze winds from the sea to the land, producing a local CO_2 maximum in the South East of the domain (Fig. 9c). Further inland, CO_2 is kept to low values by photosynthesis, with locally minimum concentrations over rice-paddy and citrus active sinks, as expected from NEE in Fig. 4. The anthropogenic CO_2 plume from the city of Valencia, becomes advected inland and channeled upward into the Turia valley, as Fig. 9c shows very clearly.

At 15:00 in the afternoon, the winds veer to the SE over the sea and the pattern of the convergence lines looks quite different from the one at 11:00, although the breeze persists (Fig. 9d). The high CO_2 concentration values from the remnants of the "drainage lake" are transported northerly across the campaign domain (compare Figs. 9c and e). Together with a gradual decrease in photosynthesis after noon, the passage of this CO_2 maximum explains why CO_2 remains approximately 1.5 ppm higher near the coast than inland.

At 18:00 in the evening, the wind direction persists from the Southeast over the sea. The wind strongly diverges over land and shifts to the Northeast in the southern part of the domain (Fig. 9e). Such a flow transition displaces the position of the mountain convergence lines, which re-organize as two "brackets" in a direction perpendicular to the coast (Fig. 9e). In the northern part of the domain, the fossil fuel CO_2 plume continues to accumulate in the Turia valley, with concentrations reaching above 373 ppm

ACPD
6, 2853–2895, 2006

EGU

downwind from the city being simulated. Note also that 18:00 represents the maximum in the local rush-hour traffic, which adds to the plume elevated concentration.

Finally at 21:00 in Fig. 9f, the nocturnal stage of the mesoscale circulation cycle begins again. The air cools sufficiently to start forming katabatic drainage winds flowing towards the sea. The simulated CO_2 rises at all points near the surface up to values greater than 367 ppm, an increase driven by ecosystem respiration.

6 Spatial gradients in time-averaged CO_2 due to mesoscale processes

In this section, we investigate how the coupling between the periodic mesoscale circulation in the Valencia basin and the CO_2 surface fluxes generates gradients in the temporally averaged CO_2 distribution during the 48 hour simulated period. Time averaged CO_2 is noted as $<CO_2>$. These gradients are hereafter referred to as "rectification gradients". Two modeled vertical cross-sections of $<CO_2>$ are shown in Figs. 10a–b. Both cross-sections are parallel to the coast and perpendicular to the main wind flow direction. One section is located 20 km offshore (Fig. 10b) and the other 20 km inland (Fig. 10a), allowing us to characterize the horizontal and vertical rectification gradients.

The cross-section over land in Fig. 10a shows a vertical rectification gradient. The respiration and fossil fuel emission of CO_2 during the nocturnal regime, when stable conditions prevail, determines the higher mean CO_2 concentration values in the lowermost 200 m. CO_2 assimilation by plants produces a $<CO_2>$ depletion aloft, which shows a broad minimum between approximately 500 m and 2000 m and is more pronounced in the northern part of the domain (Fig. 10a). This $<CO_2>$ depletion reflects the transport of photosynthesis-exposed air parcels that during the development of the combined breeze and up-slope winds towards the interior: (1) can be injected at different distances from the coast and heights above the ground and (2) are sunk by the effect of compensatory subsidence while returning aloft towards the sea. When the convergence lines are consolidated along the ridges of the coastal mountain ranges, the injection can occur higher, which explains the depletion of $<CO_2>$ in the northern

ACPD
6, 2853–2895, 2006

sector above 3000 m. The only exception to the generalized depletion in $<CO_2>$ observed at levels above 500 m is the positive signal located up-valley of Valencia. The city, emitter of fossil fuel CO_2, is the only source of positive signal active during the diurnal regime and is also exposed to the aforementioned mesoscale processes, whose effects create the increase in $<CO_2>$ inland at the lee of the city. In our study area, the 3-D character of the flow driven by mesoscale circulations explains why the $<CO_2>$ minimum compensating for the $<CO_2>$ maximum near the ground is modeled at much higher altitudes (≈1000 m) than in "classic" 1-D diurnal rectifier simulations over flat terrain (≈400 m) involving vertical dilution of photosynthesis by convective mixing (Denning, 1994; Denning et al., 1996). The specific role of breeze circulations in the vertical profile of $<CO_2>$ can also be seen by comparing the relatively modest daytime mixed layer height in Fig. 8 with the higher altitude of the mean CO_2 minimum in Fig. 10a.

Combined with this vertical rectification, there is also a horizontal rectification effect. The cross-section of $<CO_2>$ over the sea in Fig. 10b shows that positive signal concentration predominates in the lower levels and there are two regions aloft where the depletion of $<CO_2>$ is present. This horizontal pattern is related to the features shown on the inland vertical cross-section, although some differences can be observed. The smoother horizontal signals are consequence of longer distance to the sources, and the altitudes where $<CO_2>$ depletion is observed are lower due to the greater subsidence over the sea. These location-dependent behaviour differences become more evident when analyzing the simulated $<CO_2>$ integrated in the vertical and horizontal direction in Figs. 10c and f. We observe in Fig. 10c that there is a $<CO_2>$ deficit over land, coupled with a $<CO_2>$ excess over the sea. The mean excess over the sea is created by the nocturnal drainage of respired CO_2 within a shallow layer where, on the next day, it stagnates and partially becomes re-entrained back over land (Figs. 10e and 9). Most of this excess $<CO_2>$ is confined near the sea surface and over the coastal plains. Figure 10d shows the $<CO_2>$ minimum to be located at the 1000 m height. This minimum corresponds to photosynthesis-exposed air parcels that were injected into the return flow during breeze development and horizontally stratified over the sea

ACPD
6, 2853–2895, 2006

EGU

by compensatory subsidence.

Such a 3-D-rectification effect of atmospheric CO_2 can be expected in many other coastal areas with similar mesoscale circulation features. For instance, the Western Mediterranean Basin is surrounded by mountain ranges in Spain, Southern France, Italy and North Africa, which could generate similar mesoscale CO_2 transport and rectification throughout the whole basin. According our analysis, both a strong negative vertical gradient in $<CO_2>$ with increasing altitude and a large horizontal gradient in $<CO_2>$ with higher values over the sea and lower values inland could be expected as a result of the combined mesoscale effects at the WMB scale. This is very different from what a global model would simulate and, if proved to be widespread, such mesoscale effects should be considered at any station meant to measure "background" regional air.

If we seek in the future to infer local fluxes from CO_2 concentration measurements, analysis of the spatial distribution of $<CO_2>$ in Fig. 10 suggests that a sampling strategy for inverting the carbon balance of the Valencia basin, must consider taking vertical profiles of CO_2 from the ground to heights that can reach 3500 m during the afternoon. The high variability of the CO_2 concentration signal in the lower 1500 m along both vertical cross sections in Fig. 10 suggests that the measurement density should be high both spatially and temporally. One could then to take vertical profiles simultaneously over the sea and at different locations inland to capture photosynthesis sinks, and to use the drainage winds at night as a "laboratory assistant" to quantify the integrated value of the respiration sources.

7 Summary and conclusions

Consecutive vertical profiles of CO_2 concentration and meteorological parameters were collected during an intensive campaign in the Valencia region, on the western Mediterranean coast. In this region in summer, there is a marked diurnal cycle characterized by the development of a sea breeze that combines with up-valley circulations to trans-

port airmasses inland during the day (up to ≈60–100 km) and a reversal-to-seawards drainage during the night. This meteorological cycle results in an important coupling between atmospheric transport and surface CO_2 fluxes. To understand these processes and their interplay, we set up a 3-D regional mesoscale transport model, driven by meteorology calculated from the RAMS model in a companion paper. In our model, the regional distribution of NEE is estimated using a set of eddy-covariance measurements over different representative ecosystems, and transported using a particle dispersion model. The simulated CO_2 concentration field is compared with observations to elucidate the transport processes. We found that our simulation could not match the observed profiles quantitatively. This is probably because the contribution of fluxes from outside the domain via horizontal advection is ignored, and because our NEE model is very simplistic. The model-data mismatch could also reflect limitations either in mesoscale models ability to resolve layers of tenths of meters at feasible vertical resolutions, or in the applicability of available turbulence parameterizations under such conditions. Despite such biases, we nevertheless found that the model could successfully reproduce some of the crucial processes that control the mesoscale transport of CO_2. These processes are:

1) The nocturnal drainage flow from the valleys, which captures CO_2 emitted by plant and soil respiration and by fossil fuel sources. This circulation advects a shallow layer with high CO_2 concentration just above the sea at distances of up to 100 km away from the coast.

2) The diurnal flow regime, where breeze circulations transport inland signal of lower CO_2 concentrations, due to air mass exposure to vegetation uptake,

3) The vertical injections of airmasses along the convergence lines, at different distances from the coast and heights above the ground during daytime, connecting the breeze cells and bringing lower CO_2 concentration values into the return circulation branch aloft,

4) The evidence that compensatory subsidence limits the vertical dilution of the NEE daytime uptake of CO_2 by mixing and permits the formation of airmasses with strong CO_2 deficit in the atmosphere. Such a subsidence also increases the stability of the atmosphere above the mixed layer top and contributes to maintain these strong CO_2 signals aloft,

5) The coupling between the cyclic mesoscale flow reversal and the NEE diurnal cycle, which favors a splitting of regional maximum and minimum in $<CO_2>$, with a negative vertical $<CO_2>$ gradient upwards and a negative horizontal $<CO_2>$ gradient seawards, showing a 3 D rectification effect. Vertically, the depletion in $<CO_2>$ prevails between 500 and 2000 m, while in the lower levels a permanent build-up of $<CO_2>$ persists.

These processes, identified only for the selected case study, are expected to be present frequently in the atmosphere, although their interactions or intensity and the corresponding time-varying CO_2 distribution can be different each day. In general, during the warm season, we expect the flow to show a marked 3-D character and be highly sheared and in continuous transition between the different stages of the diurnal cycle capable of generating recirculation effects. This cycle can cause airmasses with different histories, different CO_2 signals and high temporal variability to be included in the same vertical profile. Such was found in the case study analyzed as well as in several CO_2 profiles measured during the two-week campaign (Hutjes et al., 2003). Meteorological analysis performed in P06 showed that the identified mesoscale processes prevail in the region every year from April to September and should be taken into account in any future study aiming to explain the variability of CO_2 during the course of a year.

Studies on air pollution in the Western Mediterranean Basin have shown that similar mesoscale circulations are present in many of the regions with coastal mountains, where interaction at different scales generates a self-organization of the flow at basin level (Millan et al., 1997; Gangoiti et al., 2001). If the simulated distribution of minimum

and maximum in the atmospheric CO_2 concentration linked to mesoscale processes in the Valencia region is boldly extrapolated to the rest of the Western Mediterranean coastal regions, a large scale of 3-D CO_2 rectification gradients could occur around the whole basin. This hypothesis could be tested by combining mesoscale model simulations with vertical CO_2 profiles collected simultaneously over the sea and inland.

Appendix A

Analysis of uncertainties in the different components of the measuring/modeling systems

A1 Uncertainties in the vertical CO_2 and H_2O measurements

In the vertical profiles, CO_2 and H_2O number densities were measured with an open-path IRGA, and then mole fractions were computed using the temperature and static pressure measured by the Mobile Flux Platform. Errors in mole fraction computations can arise from errors associated with static pressure measurement and temperature measurement, as well as from errors related to the different positions of the static pressure measurement point and the IRGA optical path.

Static pressure Ps is measured by means of a pneumatic average of four points located at 41.8 deg on the MFP sphere. Errors in Ps can arise from sensor errors and from probe design, and a detailed error analysis can be found in Crawford and Dobosy (1992) along with results with an error of less than 1% q within normal operating range, where q is the dynamic pressure, around 0.1 kPa at SkyArrow flight speed. An uncertainty of less than 0.15°K in absolute temperature measurement using the MFP equipment has also been reported by Crawford and Dobosy (1992). The IRGA optical path has a real pressure that is different from the pressure measured on the sphere because of the aerodynamic effects that occur on the IRGA body. Such a difference is a function of aircraft air speed and attitude angles, and we estimate (from computa-

ACPD
6, 2853–2895, 2006

tional fluid dynamics, data not shown) that an error of less than 0.7 KPa is associated with pressure measurements on the MFP sphere.

By combining such multiple error sources into the absolute concentration computation, an accuracy of ±3 ppm is obtained for the experimental data.

A2 Estimation of NEE

To test the approach used in this study to estimate vegetation fluxes, we performed some sensitivity tests to check the consistency of our results with respect to the simulated CO_2 vertical variations described in Sect. 4. The selection of the dry- condition days in SA to obtain the parameters in Eq. (1) was considered adequate for representing the vegetation activity under inland conditions during the campaign (Sect. 3.2). In case M+ (see Table A1) we estimated the SA parameters during the two-week campaign under normal conditions (moderate temperature and humidity). Thus, we were able to establish a high-level vegetation activity that helped us to estimate the influence of error in the flux estimation of this land use. Case C+ (C-) in Table A1 aims to represent the high (low) level activity of the Citrus orchards, where the parameters are obtained by increasing (decreasing) the CO_2 fluxes in the fitting of Eq. (1) by 50%. We consider that the parameters estimated from the eddy-covariance tower data at the rice field (Table 1) can be regarded as representative of the totality of rice fields because all the crops are located in a region under similar conditions. This was confirmed by the aircraft horizontal transects (Fig. 4).

We tested 3 cases by combining M0 and C0 (parameters according to Sect. 3.2 in both cases), M+, C+ and C- to obtain the maximum variation in the flux estimation. Figure A1 shows that the three cases present vertical distributions similar to the control case. Although there is a quantitative change in the values of the layers, the main conclusions of this study regarding the vertical distribution of CO_2 in a coastal complex terrain region are not affected.

ACPD
6, 2853–2895, 2006

EGU

A3 Estimation of the spatial distribution of sources

To check whether the source distribution established in the CO_2-transport simulation with HYPACT in Sect. 3.5 permitted a realistic distribution of the vegetation activity in the whole region, we compared it with the NDVI (Normalized Difference Vegetation Index) obtained from satellite data (SPOT 4 VEGETATION data, available at http://free.vgt.vito.be, CNES copyright) during the 10 days composite period centered in 1 July 2001 (Fig. A2). We calculated the average and the standard deviation of NDVI in each of the 19 sources configured in Sect. 3.5. It was clear that the sources that represent rice fields present the highest values of NDVI (all higher than 0.6), while the lowest values correspond to the City (0.30). The averaged values for the sources located to the north of 39.6 latitude are between 0.40 and 0.51 for both the Mosaic and Citrus categories and may be inconsistent with our study in this part. South of this latitude, Mosaic values are between 0.4 and 0.45, while Citrus are between 0.43 and 0.56. This analysis shows that the differences in vegetation activity that we established in the configuration of the sources are mostly coherent with the differences shown by the NDVI. The Mosaic category in the northern part of the region seems to be more active than we estimated. However, due to the meteorological conditions, the analysis of the source areas that contribute to the CO_2 variations described in Sect. 3, showed that 87% of the simulated CO_2 concentrations came from sources located at the south of the 39.6 latitude. Thus, the deviation of the vegetation activity in the northern part has a moderate effect on the simulated profiles.

Acknowledgements. This work has been partially supported by the projects RECAB (EVK2-CT-1999-00034) and CARBOEUROPE-IP (GOCE-CT-2003-505572), funded by the European Commission. The authors wish to thank all those who worked hard to collect the data in the field. We are grateful to D. Sotil for his support with the graphics. Also thanks to J. A. Alloza and J. V. Chordá for reclassifying CORINE and PELCOM physiography data into RAMS land use categories. J. Scheiding's corrections of the English text are appreciated. NCEP and ECMWF are acknowledged for providing meteorological analysis and reanalysis data. The CEAM foundation is supported by the Generalitat Valenciana and BANCAIXA.

References

Atkin, O. K., Bruhn, D., Hurry, V. M., and Tjoelker M.G.: The hot and the cold: unravellling the variable response of plant respiration to temperature, Funct. Plant Biol., 32, 87–105, 2005.

Aubinet, M., Grelle, A., Ibrom, A., Rannik, U., Moncrieff, J., Foken, T., Kowalski, A. S., Martin, P. H., Berbigier, P., Bernhofer, C., Clement, R., Elbers, J., Granier, A., Grunwald, T., Morgenstern, K., Pilegaard, K., Rebmann, C., Snijders, W., Valentini, R., and Vesala, T.: Estimates of the annual net carbon and water exchange of European forests: the EUROFLUX methodology, Adv. Ecol. Res., 30, 113–175, 2000.

Bousquet, P., Peylin, P., Ciais, P., LeQuere, C., Friedlingstein, P., and Tans, P.: Regional Changes in Carbon Dioxide Fluxes of Land and Oceans Since 1980, Science, 290, 1342–1346, 2000.

Caplan, P., Derber, J., Gemmill, W., Hong, S. Y., Pan, H. L., and Parish, D.: Changes to the NCEP operational medium-range forecast model analysis/forecast system, Weat. Forecasting, 12, 581–594, 1997.

CEC (Commission of the European Communities): CORINE Land cover, Guide Technique, Brussels, Available on-line, http://reports.eea.eu.int/COR0-landcover/en, 1995.

Chevillard, A., Karstens, U., Ciais, P., Lafont, S., and Heimann, M.: Simulation of atmospheric CO_2 over Europe and Siberia using the regional scale model REMO, Tellus, 54B, 872–894, 2002.

Ciais, P., Tans, P. P., Trolier, M., White, J. W. C., and Francey, R. J.: A large northern hemisphere terrestrial CO_2 sink indicated by the 13C/12C ratio of atmospheric CO_2, Science, 269, 1098–1102, 1995.

Crawford, T. L. and Dobosy, R. J.: A sensitive fast response probe to measure turbulence and heat flux from any airplane. Bound.-Layer Meteor., 59, 257–278, 1992.

De Wekker, S. F. J., Steyn, D. G., and Nyeki, S.: A comparison of aerosol layer- and convective boundary layer structure over a mountain range during STAAARTE '97, Bound.-Layer Meteor, 113, 249–271, 2004.

Denning, A. S., Collatz, J. G., Zhang, C., Randall, D. A., Berry, J. A., Sellers, P. J., Colello, G. D., and Dazlich, D. A.: Simulations of terrestrial carbon metabolism and atmospheric CO_2 in a general circulation model, Part 1: Surface carbon fluxes, Tellus, 48B, 521–542, 1996.

Denning, S.: Investigations of the transport, sources and sinks of atmospheric CO_2 using a general circulation model, PhD Thesis thesis, Colorado State University, 1994.

Falge, E., Baldocchi, D. D., Olson, R. J., Anthoni, P., Aubinet, M., Bernhofer, C., Burba, G., Ceulemans, R., Dolman, H., Granier, A., Gross, P., Grünwald, T., Hollinger, D., Jensen, N. O., Katul, G., Keronen, P., Kowalski, A. S., Ta Lai, C., Law, B. E., Meyers, T., Moncrieff, J., Moors, E., Munger, J. W., Pilegaard, K., Rannik, U., Rebmann, C., Suyker, A., Tenhunen, J., Tu, K., Verma, S., Vesala, T., Wilson, K., and Wofsy, S.: Gap filling strategies for defensible annual sums of net ecosystem exchange, Agric. For. Meteorol., 107, 43–69, 2001.

Fan, S., Gloor, M., Mahlman, J., Pacala, S., Sarmiento, J., Takahashi, T., and Tans, P.: A large terrestrial carbon sink in North America implied by atmospheric and oceanic carbon dioxide data and models, Science, 282, 442–446, 1998.

FAO: World reference base for soil resources, Food and Agriculture Organization of the United Nations, Rome, Available online at http://www.itc.nl/~rossiter/Docs/WRB/wsrr84e.pdf, 1998.

Gangoiti, G., Alonso, L., Navazo, M., Albizuri, A., Pérez-Landa, G., Matabuena, M., Valdenebro, V., Maruri, M., García J. A., and Millán M. M.: Regional transport of pollutants over the Bay of Biscay: analysis of an ozone episode under a blocking anticyclone in west-central Europe, Atmos. Environ., 36(8) 1349–1361, 2002.

Gangoiti, G., Millán, M. M., Salvador, R., and Mantilla E.: Long-range transport and re-circulation of pollutants in the western Mediterranean, during the project Regional Cycles of Air Pollution in the West-Central Mediterranean Area, Atmos. Environ., 35, 6267–6276, 2001.

Gerbig, C., Lin, J. C., Wofsy, S. C., Daube, B. C., Andrews, A. E., Stephens, B. B., Bakwin, P. S.,and Grainger, C. A.: Towards constraining regional-scale fluxes of CO_2 with atmospheric observations over a continent: 2. Analysis of COBRA data using a receptor-oriented framework, J. Geophys. Res., 108, 4757, doi:10.1029/2003JD003770, 2003.

Gioli B., Miglietta, F., De Martino, B., Hutjes, R. W. A , Dolman, H. A. J., Lindroth, A., Schumacher, M., Sanz, M. J., Manca, G., Peressotti, A., and Dumas, E. J.: Comparison between tower and aircraft-based eddy covariance fluxes in five European regions, Agric. For. Meteorol., 127, 1–16, 2004.

Gurney, K. R., Law, R. M., Denning, A. S., Rayner, P. J., Baker, D., Bousquet, P., Bruhwiler, L., Chen, Y.-H., Ciais, P., Fan, S., Fung, I. Y., Gloor, M., Heimann, M., Higuchi, K., John, J., Maki, T., Maksyutov, S., Masarie, K., Peylin, P., Prather, M., Pak, B. C., Randerson, J., Sarmiento, J., Taguchi, S., Takahashi, T., and Yuen, C.-W: Towards robust regional estimates of CO_2 sources and sinks using atmospheric transport models, Nature, 415, 626–630, 2002.

Hutjes, R., van den Bulk, W. C. M., Cosin, S., et al." : Regional Assessment and monitoring

of the carbon balance within Europe (RECAB), Final Report. Alterra, PO Box 47, 6700 AC, Wageningen. Netherlands, 2003.
Kotroni, V., Kallos, G., Lagouvardos, K., Varinou M., and Walko, R.: Numerical Simulations of the Meteorological and Dispersion Conditions during an Air Pollution Episode over Athens, Greece, Journal of Applied Meteorology: 38(4), 432–447, 1999.
Lin, J. C., Gerbig, C., Daube, B. C., Wofsy, S. C., Andrews, A. E., Vay, S. A., and Anderson, B. E.: An Empirical Analysis of the Spatial Variability of Atmospheric CO_2: Implications for Inverse Analyses and Space-borne Sensors, Geophys. Res. Lett., 31, L23104, doi:10.1029/2004GL020957, 2004.
Lu, L., Denning, A.S., da Silva-Dias, M. A., da Silva-Dias, P., Longo, M., Freitas, S. R., and Saatchi, S.: Mesoscale circulations and atmospheric CO_2 variations in the Tapajós Region, Pará, Brazil, J. Geophys. Res., 110, D21102, doi: 10.1029/2004JD005757, 2005.
Marland, G., Boden, T. A., and Andres, R. J.: Global, regional, and national CO_2 emissions in trends: A compendium of data on global change, Carbon Dioxide Information Analysis Center, Oak Ridge National Laboratory, U.S. Department of Energy, Oak Ridge, Tenn., USA, 2003.
Michaelis, L. and Menten, M. L.: Die Kinetik der Invertinwirkung. Biochemische Zeitschrift 49, 333–369, 1913.
Millán, M. M., Salvador, R., Mantilla, E., and Kallos, G.: Photooxidants dynamics in the Mediterranean basin in summer: Results from European research projects, J. Geophys. Res., 102 (D7), 8811–8823, 1997.
Millán, M. M., Artiñano, B., Alonso, L., Castro, M., Fernandez-Patier, R., and Goberna, J.: Meso-Meteorological Cycles of Air Pollution in the Iberian Peninsula, (MECAPIP), Air Pollution Research Report 44, EUR No. 14834, European Commission DG XII/E-1, Rue de la Loi, 200, B-1040, Brussels, 1992.
Nicholls, M. E., Denning, A. S., Prihodko, L., Vidale, P. L., Davis, K., and Bakwin, P.: A multiple-scale simulation of variations in atmospheric carbon dioxide using a coupled biosphere-atmospheric model,. J. Geophys. Res., 109, D18117, doi:10.1029/2003JD004482, 2004.
Olivier, J. G. J. and Berdowski, J. J. M.: Global emissions sources and sinks, in: The Climate System, edited by: Berdowski, J., Guicherit, R., and Heij, B. J., A. A. Balkema Publishers/Swets & Zeitlinger Publishers, Lisse, The Netherlands, ISBN 90-5809-255-0, 33–78, 2001.
Palau, J. L., Pérez-Landa, G., Diéguez, J. J., Monter, C., and Millán, M. M.: The importance of

meteorological scales to forecast air pollution scenarios on coastal complex terrain, Atmos. Chem. Phys., 5, 2771–2785, 2005.

Rayner, P. J., Enting, I. G., Francey, R. J., and Langenfelds, R.: Reconstructing the recent carbon cycle from atmospheric CO_2, $\delta^{13}C$, and O_2/N_2 observations, Tellus, 51B, 213–232, 1999.

Schumacher, M.: Airborne and ground level flask sampling for regional carbon budgets the potential of multiple tracer and isotope analyses, PhD. thesis, University Hamburg, http://www.sub.uni-hamburg.de/opus/volltexte/2005/2576/, 2005.

Seufert, G., Sanz, M., and Millán, M. M.: Report on the 3rd BEMA measuring campaign at Burriana (Valencia–Spain) July 12–23, 1995, Joint Research Centre Rep. EUR 17305 EN (Available from Office of Official Publications of the European Communities, L-2985, Luxemburg), 140, 1997.

Tremback, C. J., Lyons, W. A., Thorson, W. P., and Walko, R. L.: An emergency response and local weather forecasting software system, Preprints, Eighth Joint Conf. on the Applications of Air Pollution, Nashville, TN, Amer. Meteor. Soc., 219–233, 1994.

Walko, R. L., Tremback, C. J., and Bell, M. J.: HYPACT Hybrid Particle and Concentration Transport Model, Users Guide, Mission Research Corporation, Fort Collins, Colorado (USA), 2001.

Table 1. Parameters of the NEE simulation model for Mosaic, Rice and Citrus vegetation, as deduced from different eddy-covariance datasets (see text).

	Mosaic	Citrus	Rice
a_i	1.86	3	3.6
b_i	0.01642	0.025	0.03005
c_i	4.91	15	28.21

ACPD
6, 2853–2895, 2006

Table A1. Parameters of the NEE simulation model obtained for Mosaic under normal (not dry) conditions (M+) and estimated to test the sensitivity of the study to an increase of 50% (C+) and a decrease of 50% (C-) in the activity of the Citrus landuse considered.

	M+	C+	C-
a_i	2.86	4.5	1.5
b_i	0.00246	0.0375	0.0125
c_i	12.83	22.5	7.5

ACPD
6, 2853–2895, 2006

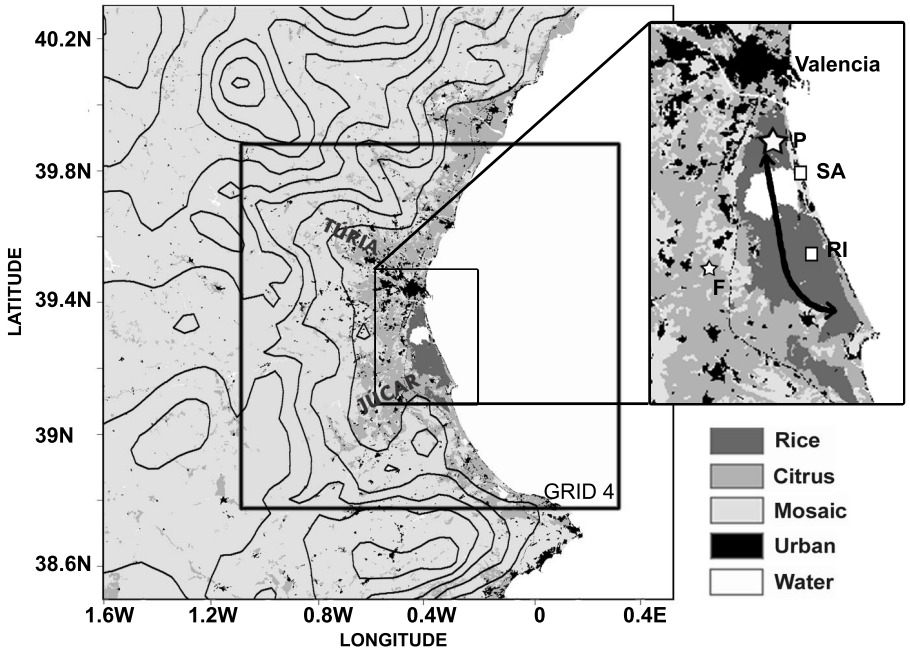

Fig. 1. Land cover types in the Valencia region (see legend). Contour lines show the orography every 200 m. The location of the smallest-domain for simulated meteorology using RAMS mesoscale model is indicated by the black solid line (Grid 4). The campaign region is zoomed to show the location of eddy-covariance flux towers (squares) at El Saler pine forest (SA) and over the rice paddies (RI), airborne horizontal transect (black arrow), vertical profile (big star, P), and flask air sampling (small star, F).

ACPD
6, 2853–2895, 2006

EGU

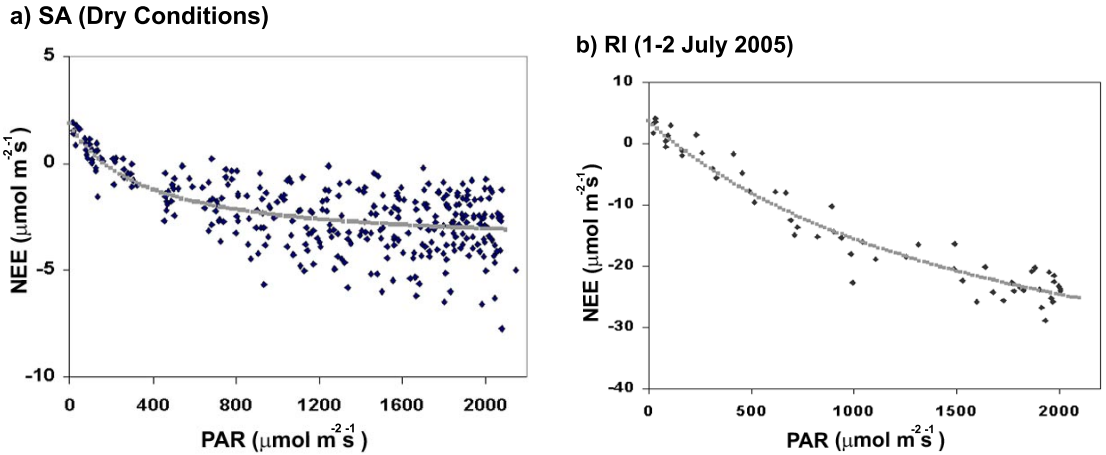

Fig. 2. Observed vegetation atmospheric CO_2 flux (NEE in μmol m^{-2}s^{-1}) as a function of solar radiation in the PAR domain (μmol m^{-2}s^{-1}): **(a)** El Saler (SA in Fig. 1) during the days selected for driest conditions between June and August 2001, **(b)** the Rice tower (RI in Fig. 1) during 1–2 July.

ACPD
6, 2853–2895, 2006

EGU

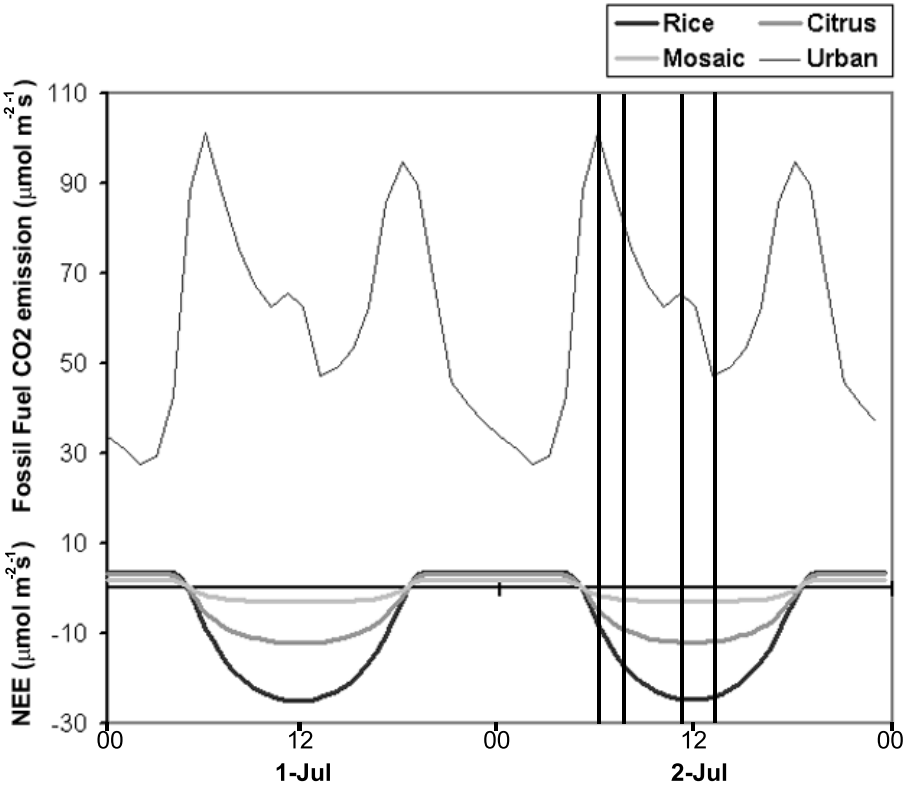

Fig. 3. CO_2 fluxes estimated according to the text, during 1 and 2 July for the different vegetation types and urban emissions (μmol m^{-2}s^{-1}). Vertical solid lines represent the times of available profiles observed on 2 July.

ACPD
6, 2853–2895, 2006

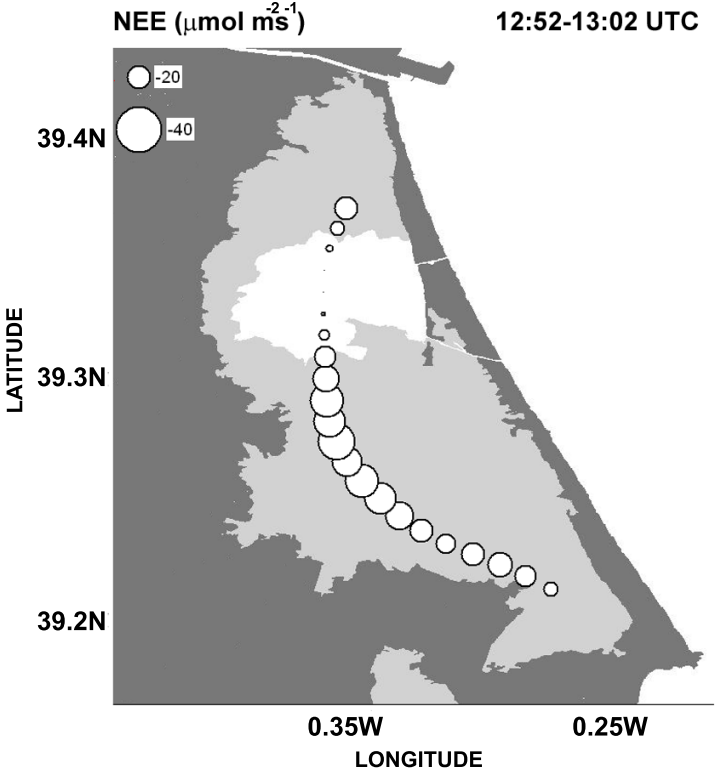

Fig. 4. Airborne CO_2 Fluxes at 25 m height over the Rice paddies measured between 12:52 and 13:02 UTC. The size of each circle is the CO_2 Flux density in μmol m^{-2}s^{-1}.

ACPD
6, 2853–2895, 2006

EGU

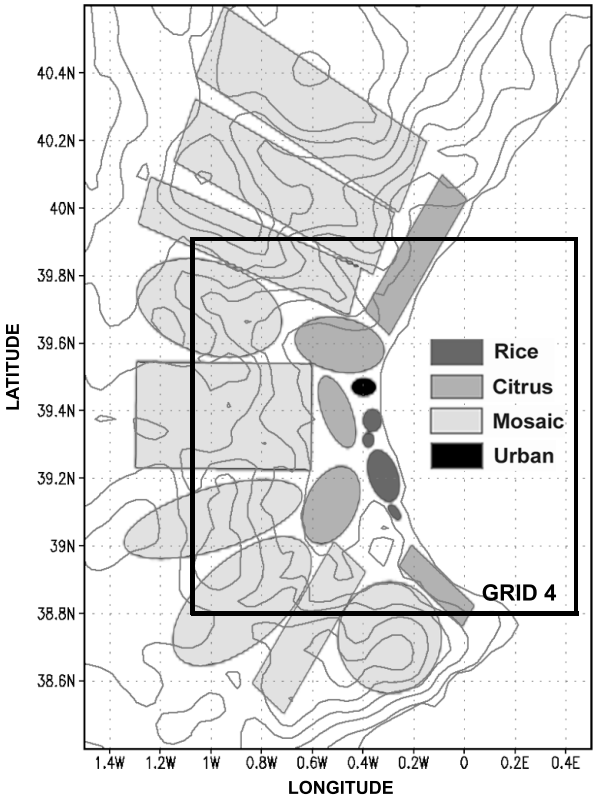

Fig. 5. Source regions considered in the particle dispersion model simulation. Each colour represents the different land-uses according to the legend.

ACPD
6, 2853–2895, 2006

EGU

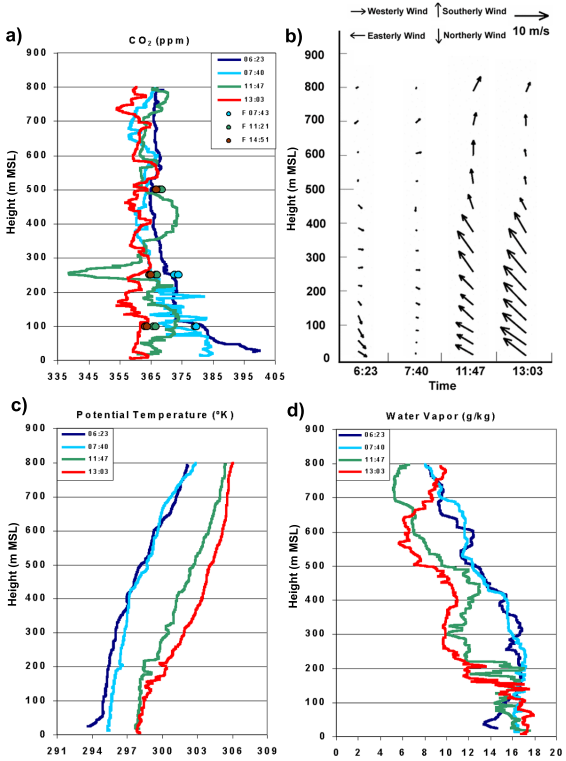

Fig. 6. Aircraft vertical profiles of **(a)** CO_2 concentration (ppm), **(b)** horizontal wind vector ($m\,s^{-1}$), **(c)** potential temperature (°K) and **(d)** water vapour ($g\,Kg^{-1}$) collected at successive intervals on 2 July of the campaign. Solid circles in (a) represent CO_2 measurements in flask air samples by another aircraft at a nearby location (see Fig. 1) at the corresponding times indicated in the legend.

ACPD
6, 2853–2895, 2006

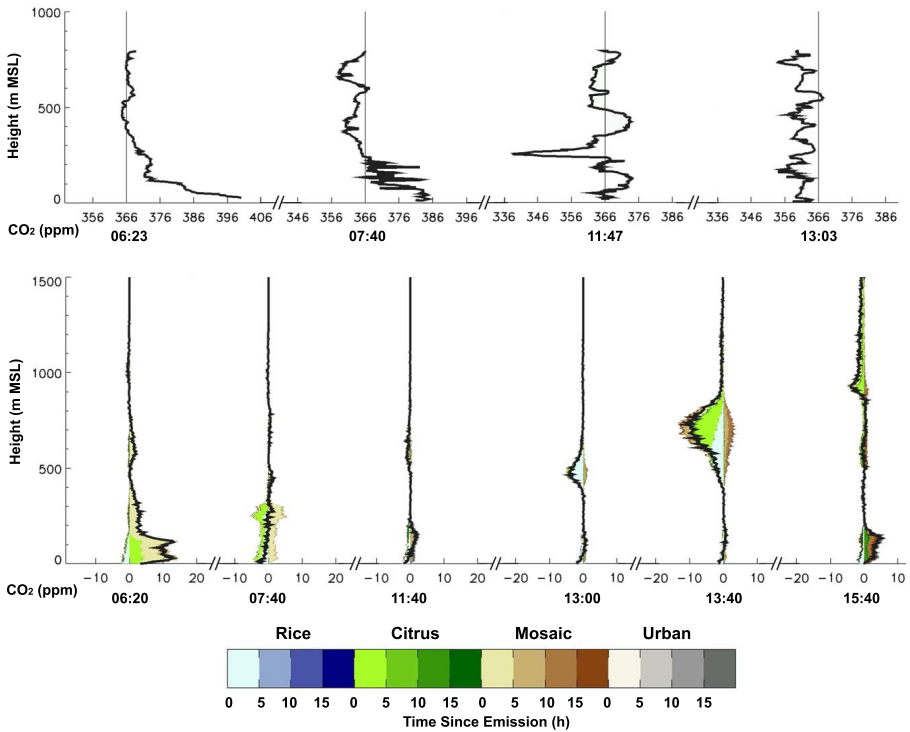

Fig. 7. Top: profiles of CO_2 (ppm) measured at P (Fig. 1) at different times on 2 July. Bottom: Simulated contribution to the simulated net CO_2 profile in P, at the corresponding time on 2 July, classified by origin and time since emission (shaded colors). Black solid line represents the net CO_2 profile obtained by adding negative and positive signals.

ACPD
6, 2853–2895, 2006

EGU

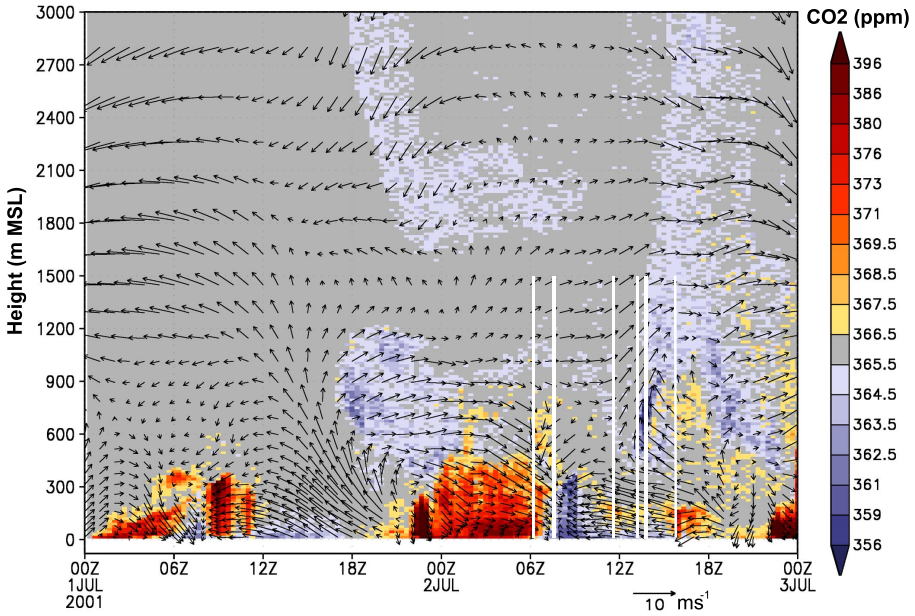

Fig. 8. Time series of the simulated profile of the lower 3 km of the atmosphere for wind (m s^{-1}) and CO_2 (ppm) at the place where continuous profiles were measured (see Fig. 1) during the 1 and 2 July. Wind arrows are plotted for every layer of the meteorological model and every hour, while CO_2 concentrations are calculated every 20 m. White solid lines represent the times of the vertical simulated profiles showed in Fig. 7. We added 366 ppm to the positive and negative simulate signal as an offset obtained from the average of the CO_2 values measured in the top of the four profiles considered in this study.

ACPD
6, 2853–2895, 2006

EGU

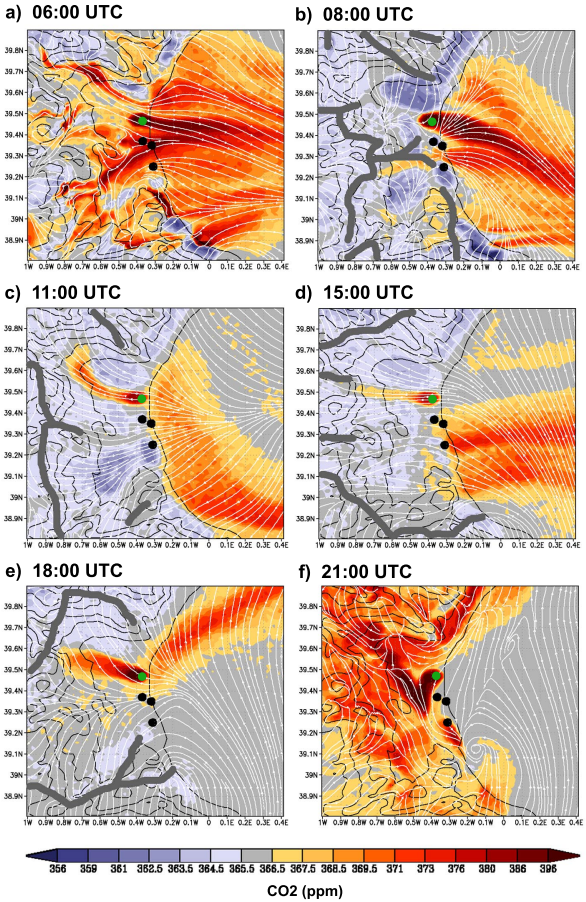

Fig. 9. Horizontal streamlines (white) and net CO_2 simulations (shaded colours) for the first level of the model at: **(a)** 06:00, **(b)** 08:00, **(c)** 11:00, **(d)** 15:00, **(e)** 18:00, **(f)** 21:00 UTC on 2 July. Dark grey solid lines represent convergence lines of the simulated horizontal wind.

ACPD
6, 2853–2895, 2006

EGU

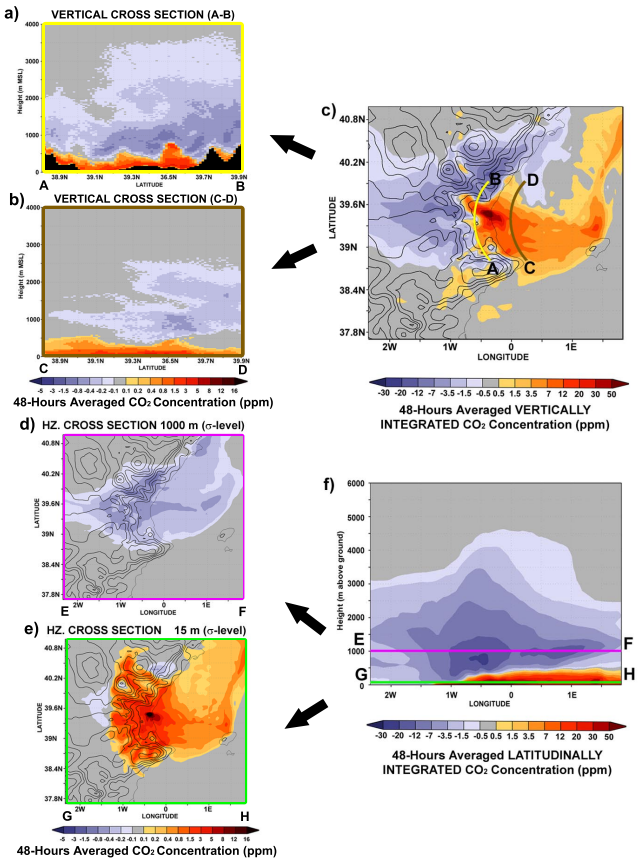

Fig. 10. 48-hour average simulated CO_2: **(a)** in the lower 4 km of the atmosphere following the inland cross-section A-B (yellow),**(b)** the sea cross-section C-D (brown), **(c)** vertically integrated in the whole regional domain, **(d)** at the 1000 m height sigma level (pink), **(e)** at the 15 m height sigma level (green) and **(f)** latitudinally integrated in the lower 6 km of the regional domain.

ACPD
6, 2853–2895, 2006

EGU

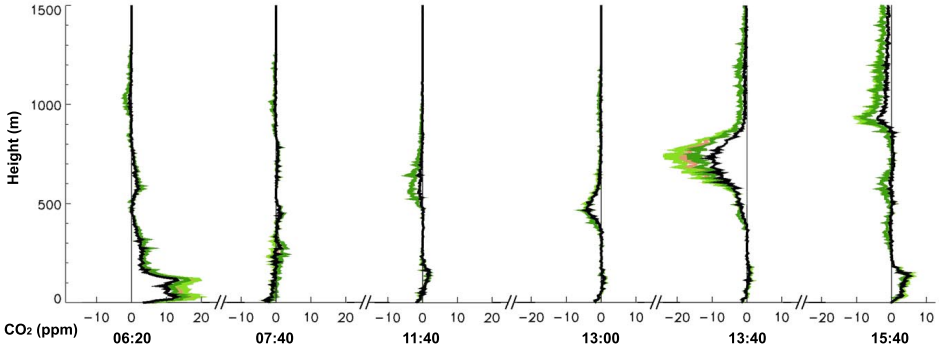

Fig. A1. Sensitivity test of simulated vertical CO_2 profiles to the NEE estimation. R0, C0 and M0 represent the Rice, Citrus and Mosaic land uses, with the parameters obtained in Sect. 3.2 and M+, C+ and C- are defined according to the text in Appendix. R0C0M0 (black) represents the control case. The three tests performed are: R0C0M+ (brown), R0C+M+ (green) and R0C-M+ (dark green).

ACPD
6, 2853–2895, 2006

EGU

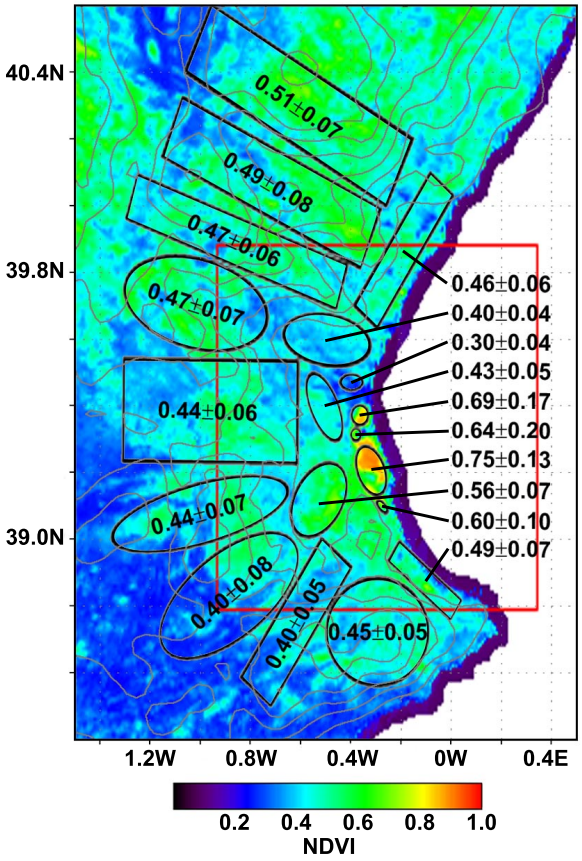

Fig. A2. NDVI estimated from satellite. Colours represent values for every pixel of 1 km^2 during the 10 days composite period centered in 1 July 2001. Numbers represent the average and standard deviation of the values in each of the 19 emission sources defined in the transport model, indicated by black solid line.